Article

# Non-Abelian braiding of Fibonacci anyons with a superconducting processor

Shibo Xu [1,7], Zheng-Zhi Sun [2,7], Ke Wang [1,7], Hekang Li [3], Zitian Zhu [1], Hang Dong [1], Jinfeng Deng [1], Xu Zhang [1], Jiachen Chen [1], Yaozu Wu [1], Chuanyu Zhang [1], Feitong Jin [1], Xuhao Zhu [1], Yu Gao [1], Aosai Zhang [1], Ning Wang [1], Yiren Zou [1], Ziqi Tan [1], Fanhao Shen [1], Jiarun Zhong [1], Zehang Bao [1], Weikang Li [2], Wenjie Jiang [2], Li-Wei Yu [4], Zixuan Song [3], Pengfei Zhang [3], Liang Xiang [3], Qiujiang Guo [3,5], Zhen Wang [1,5], Chao Song [1,5] ✉, H. Wang [1,3,5] ✉ & Dong-Ling Deng [2,5,6] ✉

Quantum many-body systems with a non-Abelian topological order can host anyonic quasiparticles. It has been proposed that anyons could be used to encode and manipulate information in a topologically protected manner that is immune to local noise, with quantum gates performed by braiding and fusing anyons. Unfortunately, realizing non-Abelian topologically ordered states is challenging, and it was not until recently that the signatures of non-Abelian statistics were observed through digital quantum simulation approaches. However, not all forms of topological order can be used to realize universal quantum computation. Here we use a superconducting quantum processor to simulate non-Abelian topologically ordered states of the Fibonacci string-net model and demonstrate braidings of Fibonacci anyons featuring universal computational power. We demonstrate the non-trivial topological nature of the quantum states by measuring the topological entanglement entropy. In addition, we create two pairs of Fibonacci anyons and demonstrate their fusion rule and non-Abelian braiding statistics by applying unitary gates on the underlying physical qubits. Our results establish a digital approach to explore non-Abelian topological states and their associated braiding statistics with current noisy intermediate-scale quantum processors.

The discovery of topological order[1] has revolutionized the understanding of quantum matter based on the Landau–Ginzburg symmetry-breaking paradigm[2]. Different topologically ordered phases could bear exactly the same symmetries and showcase topologically distinct features, such as long-range entanglement and the emergence of quasiparticles with anyonic braiding statistics[3–6]. They are of fundamental importance in understanding strongly correlated quantum phases of matter, and promise crucial applications in fault-tolerant quantum computing as well[7].

Owing to their intrinsic non-local nature, logical code spaces immune to arbitrary local perturbations can be constructed from the topological degrees of freedom of the system, and logical operations can be implemented by creating, braiding and fusing anyons. In general, the braiding of two anyons can be described by either Abelian or non-Abelian statistics, which leads to a complex phase factor or a unitary matrix acting on the degenerate-state manifold, respectively. Non-Abelian anyons are quasiparticle excitations in topologically ordered systems

[1]Zhejiang Key Laboratory of Micro-Nano Quantum Chips and Quantum Control, School of Physics, Zhejiang University, Hangzhou, China. [2]Center for Quantum Information, Institute for Interdisciplinary Information Sciences, Tsinghua University, Beijing, China. [3]ZJU-Hangzhou Global Scientific and Technological Innovation Center, Zhejiang University, Hangzhou, China. [4]Theoretical Physics Division, Chern Institute of Mathematics and LPMC, Nankai University, Tianjin, China. [5]Hefei National Laboratory, Hefei, China. [6]Shanghai Qi Zhi Institute, Xuhui District, China. [7]These authors contributed equally: Shibo Xu, Zheng-Zhi Sun, Ke Wang. ✉e-mail: chaosong@zju.edu.cn; hhwang@zju.edu.cn; dldeng@tsinghua.edu.cn
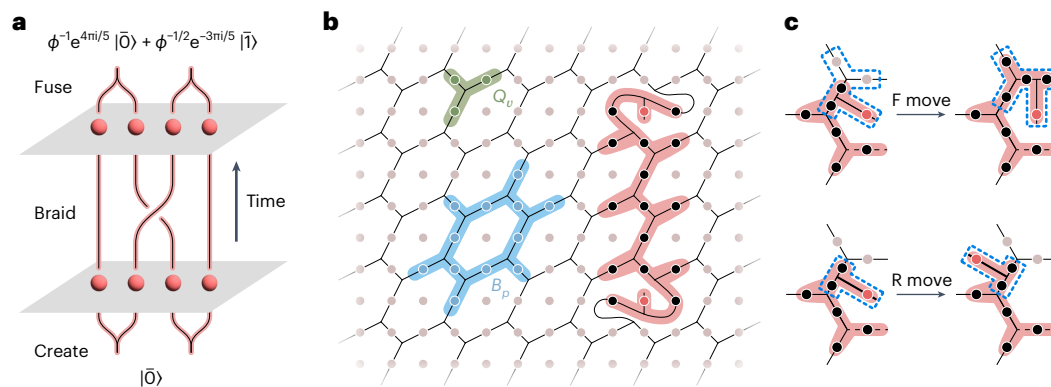
Fig. 1 | Fibonacci anyon and string-net model. a, World line of braiding Fibonacci anyons. We create two pairs of Fibonacci anyons from vacuum, braid the middle two and then fuse them. In terms of topological quantum computing, such a braid will transfer the initial logical state $|\bar{0}\rangle$ to the logical state $|\Psi\rangle_L = \phi^{-1}e^{4\pi i/5}|\bar{0}\rangle + \phi^{-1/2}e^{-3\pi i/5}|\bar{1}\rangle$, which can be detected by measuring the fusion results of the two pairs of anyons. **b**, Fibonacci string-net model is defined on a honeycomb lattice, which, in turn, is constructed out of the underlying square lattice that depicts the geometry for the transmon qubits of our quantum processor. The Q_v and B_p operators are three- and twelve-body projectors acting on the qubits associated with each vertex and plaquette, as highlighted in olive and blue, respectively. A pair of Fibonacci anyons can be created at the endpoints (red dots) of an open string operator (coral line), which can be extended and turned around by F and R moves. **c**, Effects of F move (up) and R move (down). The F-move (R-move) operator acts on five (three) qubits circled by the dashed lines, which extends (adjusts the direction of) the string operator and moves the Fibonacci anyon along (across) the plaquettes (Methods and Supplementary Section I.E).

that obey non-Abelian braiding statistics. They are the building blocks of topological quantum computing[8].

Realizing non-Abelian topologically ordered states and their associated non-Abelian anyons has been a long-sought-after goal in condensed-matter physics[8,9]. Exciting progresses have been made in both theory[10–15] and experiment[16–21]. Yet, the direct observation of non-Abelian exchange statistics has remained elusive so far. In recent years, notable advances have been achieved towards the fabrication of programmable quantum platforms such as superconducting circuits[22–25], Rydberg atomic arrays[26], photons[27,28] and trapped ions[29,30], giving rise to unprecedented opportunities in the synthesis and exploration of increasingly complex topological quantum states[31–34]. Along this direction, non-Abelian statistics has been recently observed by simulating the projective Ising anyons in the toric-code model[35,36] and creating the ground-state wavefunction of non-Abelian D_4 topological order[37]. However, neither of the braidings of anyons realized in these experiments alone sustain a universal gate set. The Ising anyons are related to the Witten–SU(2)–Chern–Simons theory at level $k = 2$, where the SU(2) model is computationally universal for $k = 3$ or $k \geq 5$ (ref. 38). For the quantum double model of the finite group (including D_4), the gate set realized by braiding is finite and is not universal[39]. With current noisy intermediate-scale quantum processors, realizing topological orders hosting non-Abelian anyons with universal computational power demands an elaborate design of device-adapted quantum circuits combined with the state-of-the-art gate fidelity and coherence time, which is exceedingly challenging and has evaded experiment thus far.

Here we report the experimental realization of Fibonacci string-net states[6,40], which are predicted to host non-Abelian Fibonacci anyons carrying universal computational power[41] (Fig. 1a), with 27 superconducting transmon qubits. We upgrade our device by optimizing the device fabrication and controlling process, and execute efficient quantum circuits obtained by variational algorithms to prepare the desired non-Abelian ground state of the string-net Hamiltonian. We measure the multi-body vertex and plaquette operators, yielding average expectation values of 0.94 and 0.58, respectively. The topological order of the prepared states is characterized by measuring the topological entanglement entropy, whose averaged value reaches −0.82, which is well below zero (for a topologically trivial state), and −0.69 (for the Z_2 topologically ordered toric-code state). In addition, we create two pairs

of Fibonacci quasiparticle excitations by acting string operators on the prepared ground state and demonstrate their non-trivial mutual statistics by braiding them with sequences supporting universal single-qubit logic gates. We extract the characterizing monodromy matrix and the quantum dimension of the Fibonacci anyon from the measured fusion results, which unambiguously indicates that the quasiparticle excitations created in our experiment are indeed Fibonacci anyons.

Framework and experimental setup

We consider the Fibonacci string-net model—the Levin–Wen model—which is the simplest string-net model supporting braiding-universal topological quantum computing[6]. The corresponding Hamiltonian is defined on a honeycomb lattice with spins living on the edges (Fig. 1b):

$$H = -\sum_v Q_v - \sum_p B_p, \qquad (1)$$

where Q_v denotes the three-body vertex operator that constrains the string types meeting at a trivalent vertex, and B_p denotes the twelve-body plaquette operator that measures the 'magnetic flux' through a plaquette and provides the dynamics for string-net configurations[6]. The ground state of H is topologically ordered and satisfies $\langle Q_v \rangle = \langle B_p \rangle = 1$ for all vertices v and plaquettes p. The quasiparticle excitations are Fibonacci anyons satisfying the following fusion rule:

$$\tau \times \tau = \mathbf{1} + \tau, \qquad (2)$$

where $\mathbf{1}$ and τ denote the vacuum and Fibonacci anyon, respectively. They can be created and manipulated by string operators[42] (Fig. 1b,c). Apparently, preparing the ground state of H and manipulating Fibonacci anyons pose a serious challenge due to the intricate multi-body plaquette operators involved in the model. To overcome this difficulty, we optimize our device and exploit efficient quantum circuits, which are obtained through the variational unitary synthesis technique[43], to prepare the desired non-Abelian ground state and use the idea of digital quantum simulation to implement creations and braidings of Fibonacci anyons (Methods and Supplementary Section III).

Our experiments are performed on a flip-chip superconducting quantum processor with frequency-tunable transmon qubits arranged
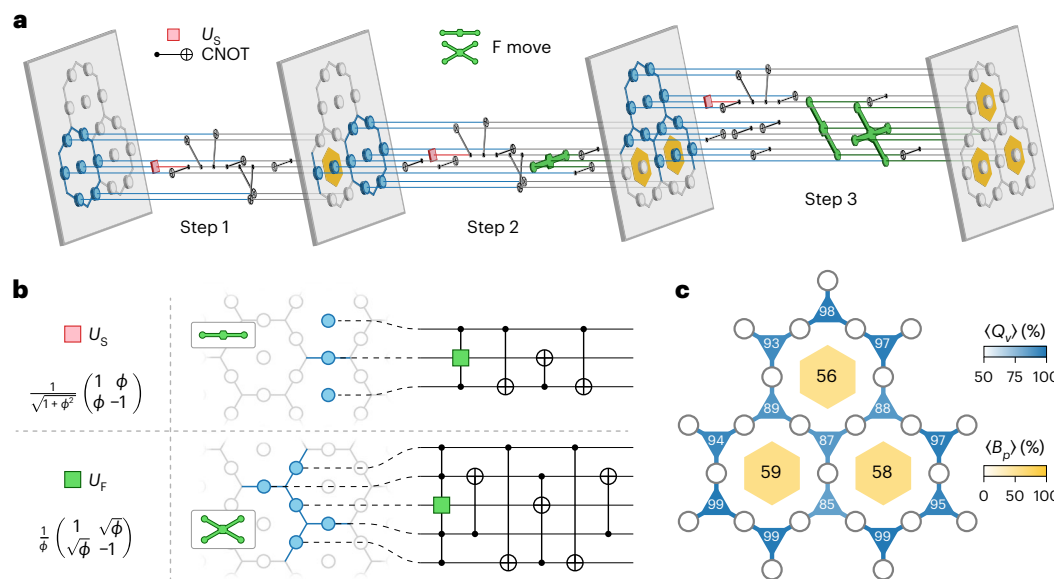
Fig. 2 | Ground-state preparation. a, Illustrative quantum circuit for preparing the ground state with time flowing to the right. Starting with all the qubits in the $|0\rangle$ state, we project each plaquette to the ground state of the corresponding B_p operator in an order indicated by the yellow hexagons. The circuit consists of single-qubit gate U_S, CNOT gates and F-move gates, which will be decomposed further into elementary gates that are native to our quantum processor. **b**, Quantum circuits for implementing the F moves shown in **a**. **c**, Measured $\langle Q_v \rangle$ and $\langle B_p \rangle$ for the non-Abelian topological ground state prepared in our experiment. A repetition number of 3,000 (300,000) is used to obtain the probability distributions on the computational basis, which are corrected with iterative Bayesian unfolding methods[58,59] to mitigate the readout error for obtaining $\langle Q_v \rangle$ ($\langle B_p \rangle$).

in a square lattice[36]. We select 27 neighbouring qubits and construct a honeycomb lattice with three plaquettes out of the underlying square lattice (Extended Data Fig. 1). The qubits living on the edges of the honeycomb lattice are used for implementing the string-net Hamiltonian H, and the other ones serve as ancillary qubits to facilitate the implementation of multi-qubit string operators. Arbitrary single-qubit gates can be realized for each qubit, whereas two-qubit controlled-Z gates can be implemented on an arbitrary neighbouring qubit pair connected by a tunable coupler. By optimizing the device fabrication and controlling process, we push the median lifetime of these qubits to 117 μs and the median simultaneous single- and two-qubit gate fidelities to around 99.96% and 99.50%, respectively. This enables us to successfully prepare the desired non-Abelian topological ground state of H and implement the braidings of Fibonacci anyons with quantum circuits of depths up to 100. Supplementary Section III.A provides the calibration procedures and detailed parameters of the device.

Ground-state preparation

We prepare the ground state of H by utilizing the fact that all Q_v and B_p are projectors commuting with each other. Noting that the N-qubit product state $|0\rangle^{\otimes N}$ is an eigenstate of all Q_v, the ground state $|G\rangle$ can be expressed as

$$|G\rangle \propto \prod_p B_p |0\rangle^{\otimes N} = \prod_p \frac{1}{1+\phi^2}\left(B_p^0 + \phi B_p^1\right)|0\rangle^{\otimes N}, \quad (3)$$

where B_p^s with $s \in \{0, 1\}$ is a twelve-body plaquette operator and $\phi = (\sqrt{5}+1)/2$ is the golden ratio. For an independent type-0 string loop $|0\rangle \otimes \cdots \otimes |0\rangle$, the B_p^0 operator leaves the configuration unchanged, whereas the B_p^1 operator changes it to a type-1 string loop $|1\rangle \otimes \cdots \otimes |1\rangle$ according to the fusion rule $\mathbf{1} \times \tau = \tau$ (ref. 6). Thus, the projector B_p for isolated string loops acting on the initial state $|0\rangle^{\otimes N}$ can be implemented by randomly choosing one qubit from the plaquette p, preparing it onto the state $\frac{1}{\sqrt{1+\phi^2}}(|0\rangle + \phi|1\rangle)$ first with a single-qubit gate $U_S = \frac{1}{\sqrt{1+\phi^2}}\begin{pmatrix} 1 & \phi \\ \phi & -1 \end{pmatrix}$ and then successively applying controlled-NOT

(CNOT) gates on the rest of the qubits, with the chosen qubit being the control qubit. Furthermore, we use the F moves to entangle different isolated loops. The ground state can be prepared by creating isolated loops and entangling them in the honeycomb lattice layer by layer. Such an approach is efficient, in the sense that the circuit depth scales only linearly with the number of plaquettes (Methods)[36,44].

The quantum circuit for the step-by-step preparation of a three-plaquette ground state is sketched in Fig. 2a, which is composed of single-qubit U_S gates, CNOT gates and F-move gates. The F-move gates can be further decomposed into multi-qubit-controlled unitary gates and CNOT gates (Fig. 2b). In our experiments, further compilations are required to fit the circuit to the nearest-neighbour geometry of our quantum device with native gates (that is, arbitrary single-qubit gates and the two-qubit controlled-Z gate). However, direct decomposition of the five-qubit F move is expensive and would result in a circuit with a depth of around 200 to prepare the ground state, which is impractical to reliably implement with a system size as large as 27 qubits for the state-of-the-art superconducting processors. We elude this dilemma by exploiting a variational approach[43] (Methods) to efficiently implement the three- and five-qubit F-move operations. The process infidelity between the synthetic unitary U and target unitary V, which is defined as $1 - \frac{|\mathrm{Tr}(U^\dagger V)|}{4^n}$, where n is the qubit number, is optimized to be below 10^{-5}. We note that this variational approach is device adapted and can substantially suppress the circuit depth for implementing F moves. Its scalability is also assured by the fact that F moves act locally and we only need to variationally approximate the F moves up to five qubits.

With this greatly simplified implementation of F moves, we first prepare the ground state of H step by step (Fig. 2a). We measure the expectation values of Q_v and B_p after each step, with the results shown in Extended Data Fig. 2. Although all the Q_v operators are diagonal in the computational basis and hence can be directly measured in the experiment, the B_p operators involve 99,328 twelve-body Pauli terms in decomposition and require 290 twelve-body measurements under different Pauli bases. The average values of Q_v and B_p after preparing
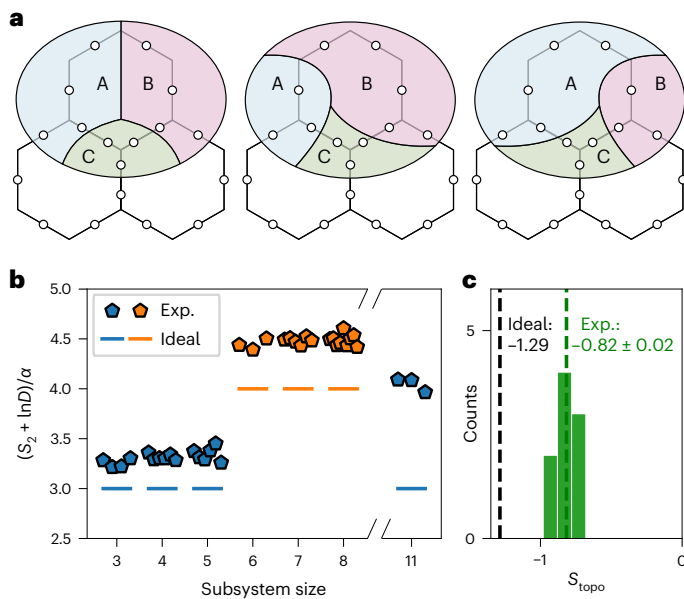
Fig. 3 | Topological entanglement entropy. a, Simply connected subregions A, B and C used to measure the topological entanglement entropy S_{topo}. For the eleven-qubit subsystem selected, there are three legitimate divisions of A, B and C. In addition, there are three different orientations of the eleven-qubit subsystem. Thus, from a single randomized measurement on all the eighteen qubits, we have nine different estimates of S_{topo}, which will converge to each other in the thermodynamic limit. **b**, Distribution of the rescaled second Rényi entropy S_2 measured for all the involved subsystems. The pentagon dots show the experimental data and lines indicate the corresponding ideal theoretical values. The entropies of subsystems with boundary lengths of three and four are coloured in blue and orange, respectively. The data are rescaled to reflect the area-law entanglement, where $\alpha \approx 0.94$ is the rescaling factor specified by the Fibonacci string-net model[46]. **c**, Distribution of the nine extracted topological entanglement entropies, with an average value of −0.82 (green dashed line). The error bar denotes the standard error of the mean. The black dashed line indicates the ideal theoretical value. Supplementary Section III.C provides more detailed error analyses of the data.

the three-plaquette ground state are 0.88 and 0.36, respectively. For the preparation of the three-plaquette ground state, we can further simplify the circuit to a depth of 53 by directly targeting the final state instead of the whole unitary during the variational search, which can generate a state with an infidelity to the target state as low as 10^{-5} in theory. We prepare the ground state with this further simplified circuit as well. The measured expectation values of Q_v and B_p are displayed in Fig. 2c, with average values of 0.94 and 0.58, respectively. These apparently larger-than-zero values indicate that the non-Abelian topological state prepared in our experiment indeed has a large overlap with the ideal ground state of H, showing the efficiency and effectiveness of our approaches. In the following, we use the prepared ground state through the further simplified circuit to study the exotic properties of the Fibonacci string-net model, including distinct topological entanglement entropy and braiding statistics of Fibonacci anyons.

Topological entanglement entropy

To characterize the topological order of the prepared ground state $|G\rangle$, we measure its topological entanglement entropy, which is a universal constant reflecting the topological properties of entanglement that survive at arbitrarily long distances[45,46]. We deliberately choose three subregions A, B and C (Fig. 3a), and the topological entanglement entropy (denoted as S_{topo}) can then be obtained through

$$S_{topo} = S_A + S_B + S_C - S_{AB} - S_{BC} - S_{AC} + S_{ABC}, \qquad (4)$$

where AB indicates the union of A and B and $S_I(I = A, B, C, AB, BC, AC, ABC)$ denotes the von Neumann entanglement entropy of a subsystem I: $S_I = -\text{Tr}(\rho_I \ln \rho_I)$, where ρ_I is the reduced density matrix. For the string-net model considered in our experiment, it is necessary to map the wavefunction to a new lattice with two qubits per boundary edge so that the partitioning can be implemented in a symmetric way[46]. From the perspective of topological quantum field theory, S_{topo} is directly related to the total quantum dimension D of the medium by $S_{topo} = -\ln D$ (refs. 45,46). For the Fibonacci string-net model, we have $D = 1 + d_\tau^2$, where $d_\tau = \phi$ is the quantum dimension of a Fibonacci anyon.

Directly measuring S_{topo} requires quantum state tomography in general, which is resource consuming and impractical for the system size considered in this work. Alternatively, one can measure the second-order Rényi entropy, from which S_{topo} can be estimated up to an exponentially small deviation for the Fibonacci string-net model[47]. In our experiment, we adopt this approach and exploit the recently developed randomized measurement method to attain S_{topo} (refs. 33,48,49). We extend the ground state to a new lattice by copying the three qubits (labelled by $Q_{(7,11)}$, $Q_{(7,13)}$ and $Q_{(5,11)}$) on the common boundary edges of the three plaquettes to the neighbouring free qubits ($Q_{(9,13)}$, $Q_{(5,13)}$ and $Q_{(5,9)}$) with CNOT gates; therefore, each common edge is associated with two qubits and can be symmetrically separated into different subsystems[46] (Methods and Supplementary Section I.G). The numbers in the subscript of Q denote the row and column indices of the corresponding qubits (Extended Data Fig. 1).

Our results are summarized in Fig. 3b,c. In Fig. 3b, we plot the distributions of the measured entanglement entropies of all the subsystems involved, with qubit numbers ranging from three to eleven. Ideally, the entanglement entropy of a subsystem scales linearly with its boundary, which is a reminder of the area-law entanglement[50] satisfied by the ground state $|G\rangle$. In our experiment, all the measured entanglement entropies are slightly above the predicted values, which is consistent with numerical estimates considering the control and decoherence errors obtained during the calibration procedures (Supplementary Section III). The nine extracted S_{topo} estimates are also slightly above the predicted value (Fig. 3c). The mean value of the measured S_{topo} is −0.82, which is significantly lower than zero (for the topologically trivial state) and $-\ln 2 \approx 0.69$ (for the Z_2 topologically ordered state). This provides strong evidence for the Fibonacci topological order of the ground state $|G\rangle$.

Braiding statistics

The topological order realized above supports a coveted type of quasiparticle—the Fibonacci anyons—whose braiding statistics can give rise to universal topological quantum computation[8]. To demonstrate the non-trivial braiding statistics of Fibonacci anyons, we create two pairs of them from vacuum living on two plaquettes (Fig. 4a). We then braid them following different sequences by the corresponding string operators. After braiding, we fuse them pairwise and measure the fusion outcomes to detect their braiding statistics. We encode a logical qubit into four Fibonacci anyons as $|\bar{0}\rangle = |(\tau \times \tau)_{\mathbf{1}}, (\tau \times \tau)_{\mathbf{1}}\rangle$ and $|\bar{1}\rangle = |(\tau \times \tau)_\tau, (\tau \times \tau)_\tau\rangle$, and denote the braiding operations of the first and middle two anyons as σ_1 and σ_2, respectively (Fig. 4b). We note that σ_1 and σ_2 are unitary logical gates and their matrix representation can be calculated by the F and R moves (Methods and Supplementary Section I.B).

Starting with the prepared ground state, we create two pairs of Fibonacci anyons labelled as $\tau_{1,2,3,4}$ by acting on two short type-1 open strings. In the logical space, we initialize the system into state $|\bar{0}\rangle$. We consider five different braiding sequences (Fig. 4c) and plot the corresponding measured fusion results in Fig. 4d(i). (1) Without braiding: as shown in Fig. 4d(i), we measure a probability of 0.81 and 0.04 for both pairs fusing to **1** and τ, respectively, which confirms the theoretical prediction that anyons created in pairs from vacuum will annihilate back into the vacuum without braiding. (2) Braiding of the middle two
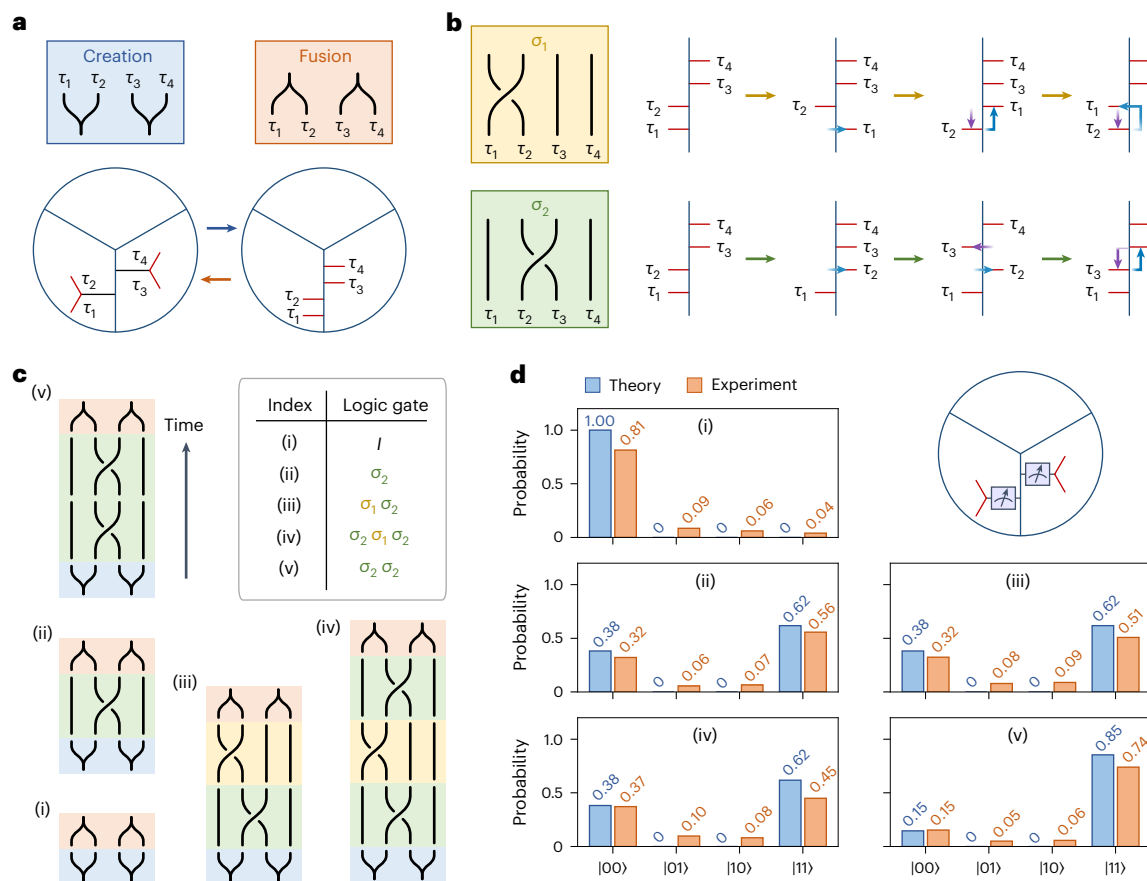
Fig. 4 | Braiding statistics. a, Creation and fusion of Fibonacci anyons, which can be described by the world lines (top), with time flowing from down to up. The corresponding operations in the string-net picture are shown in the bottom panel, where two pairs of Fibonacci anyons can be created and fused with two F moves and their inverses, respectively. The four anyons are labelled as $\tau_{1,2,3,4}$ and the fan sectors sketch the original hexagon plaquettes. **b**, World-line representation and the corresponding string-net picture for the two braiding operations σ_1 (up) and σ_2 (down). We use R moves to transfer the anyons across different plaquettes, and F moves to move them along the edge (right panel). **c,d**, Five braiding sequences (**c**) and the fusion results of Fibonacci anyon pairs at the end of each braiding (**d**). To demonstrate the braiding statistics, we create

two pairs of Fibonacci anyons from vacuum, braid them along five different paths and then fuse them. Although the direct fusion of two anyon pairs right after their creation would lead the system back to vacuum (i), other braiding sequences will result in non-trivial fusion results ((ii)–(v)). In particular, we prepare the system into an eigenstate of σ_2 by applying $\sigma_1\sigma_2$ on the ground state (iii), which is verified by the similar fusion results observed after applying $\sigma_2\sigma_1\sigma_2$ on the ground state (iv). In addition, we can also extract the monodromy matrix by applying $\sigma_2\sigma_2$ and measuring the fusion result (v). The fusion results are obtained by measuring the two physical qubits ($Q_{(5,13)}$ and $Q_{(5,9)}$; Extended Data Fig. 1) corresponding to the two string types (top-right corner in **d**) (Methods and Supplementary Section I.E).

Fibonacci anyons once: this will change the fusion output for both pairs, resulting in a superposition state in the logical space as $\sigma_2\left|\bar{0}\right\rangle = \phi^{-1}e^{4\pi i/5}\left|\bar{0}\right\rangle + \phi^{-1/2}e^{-3\pi i/5}\left|\bar{1}\right\rangle$. In our experiment, the measured probabilities of the two pairs after braiding fusing to **1** and τ are 0.32 and 0.56, respectively. This agrees with the theoretical prediction and verifies the non-Abelian fusion rule in equation (2); (3) and (4) preparation and verification of a logical eigenstate of σ_2 through braidings: from the Yang–Baxter equation[51,52], $\sigma_1\sigma_2\left|\bar{0}\right\rangle$ is an eigenstate of σ_2. This is verified by our experimental result that the difference between the fusion results before and after implementing an additional σ_2 on $\sigma_1\sigma_2\left|\bar{0}\right\rangle$ is negligible (Fig. 4d(iii),(iv)); (5) braiding of the middle two Fibonacci anyons twice, which provides information about the monodromy matrix M that characterizes the mutual statistics of Fibonacci anyons from the perspective of modular tensor category theory[40]. The elements of M can be written in the form of a logical observable as $M_{\tau\tau} = \left\langle\bar{0}\right|\sigma_2\sigma_2\left|\bar{0}\right\rangle$, where $M_{11}, M_{1\tau}$ and $M_{\tau1}$ equal 1 since the braiding with vacuum **1** does not change the fusion results. From the experimental result shown in Fig. 4d(v), we obtain that $M_{\tau\tau} = -0.39$, which agrees well with the theoretical value of $-1/\phi^2 \approx -0.38$. The measured quantum dimension of the Fibonacci anyon is $\phi_{exp} = 1.60$, very close to the ideal

value of $d_\tau = \phi \approx 1.618$. This gives a piece of clear evidence that the quasiparticle excitations we created in the experiment are indeed Fibonacci anyons. We note that a logical Hadamard gate has recently been implemented by simulating braiding sequences of boundary Fibonacci anyons with two nuclear spin qubits[53].

We mention that the braidings carried out in our experiment involve no Hamiltonian dynamics of quasiparticle excitations. As a result, they are not endowed with topological protection that naturally arises from an energy gap separating the many-body degenerate ground states from the low-lying excited states. This is distinct from conventional protocols for braiding anyons[8], and therefore, our experiment is more of a quantum simulation of braiding Fibonacci anyons in this sense. This also explains the evident small deviations between the experimentally measured fusion results after braidings and the ideal theoretical predictions. Without topological protection, inevitable experimental imperfections including gate errors and limited coherence time would cause a sizable infidelity for the final states after braidings. To leverage the Fibonacci anyons in our experiment for topologically protected quantum computing, an active error correction procedure such as the Fibonacci Turaev–Viro code[54] must

be enforced during the braiding process. We leave this interesting and important topic for future study.

Conclusion and outlook

In summary, we have experimentally prepared the ground state of the Fibonacci string-net model with non-Abelian topological order on a programmable superconducting quantum processor. We demonstrated the creation, braiding and fusion of Fibonacci anyons by applying appropriate string operators on the prepared ground state. Unlike Ising-type anyons[35,36] and those related to the D_4 topological order[37], the Fibonacci anyons demonstrated in our experiment support universal topological quantum computing. Combined with the potential inclusion of the error correction procedure[54] in the future, our results pave an alternative path towards fault-tolerant quantum computation.

The controllability of the superconducting platform and the effectiveness of our variational approach in simplifying the quantum circuits demonstrated in our experiment open up several new avenues for future studies of other exotic topologically ordered states of matter, as well as their related non-Abelian quasiparticle excitations with peculiar braiding statistics. In particular, it would be interesting and important to implement the generalized string-net models that break tetrahedral[55] or time-reversal symmetry[40], admit symmetry-enriched topological orders[56] and others described by unitary fusion categories with fusion multiplicities[57]. Experimental realizations of such topologically ordered non-Abelian states would not only deepen our understanding of these unconventional phases of matter but also provide valuable guidance for potential applications.

Online content

Any methods, additional references, Nature Portfolio reporting summaries, source data, extended data, supplementary information, acknowledgements, peer review information; details of author contributions and competing interests; and statements of data and code availability are available at https://doi.org/10.1038/s41567-024-02529-6.

References

1. Wen, X.-G. *Quantum Field Theory of Many-Body Systems: From the Origin of Sound to an Origin of Light and Electrons* (Oxford Univ. Press, 2004).
2. Landau, L. D. & Lifshitz, E. M. *Statistical Physics* Vol. 5 (Elsevier, 2013).
3. Arovas, D., Schrieffer, J. R. & Wilczek, F. Fractional statistics and the quantum Hall effect. *Phys. Rev. Lett.* **53**, 722–723 (1984).
4. Wen, X. G. Topological orders in rigid states. *Int. J. Mod. Phys. B* **4**, 239–271 (1990).
5. Wen, X. G. & Niu, Q. Ground-state degeneracy of the fractional quantum Hall states in the presence of a random potential and on high-genus Riemann surfaces. *Phys. Rev. B* **41**, 9377 (1990).
6. Levin, M. A. & Wen, X.-G. String-net condensation: a physical mechanism for topological phases. *Phys. Rev. B* **71**, 045110 (2005).
7. Kitaev, A. Y. Fault-tolerant quantum computation by anyons. *Ann. Phys.* **303**, 2–30 (2003).
8. Nayak, C., Simon, S. H., Stern, A., Freedman, M. & Das Sarma, S. Non-Abelian anyons and topological quantum computation. *Rev. Mod. Phys.* **80**, 1083 (2008).
9. Stern, A. Non-Abelian states of matter. *Nature* **464**, 187–193 (2010).
10. Moore, G. & Read, N. Nonabelions in the fractional quantum Hall effect. *Nucl. Phys. B* **360**, 362–396 (1991).
11. Alicea, J., Oreg, Y., Refael, G., von Oppen, F. & Fisher, M. P. Non-Abelian statistics and topological quantum information processing in 1D wire networks. *Nat. Phys.* **7**, 412–417 (2011).
12. Ivanov, D. A. Non-Abelian statistics of half-quantum vortices in *p*-wave superconductors. *Phys. Rev. Lett.* **86**, 268 (2001).
13. Bonderson, P., Kitaev, A. & Shtengel, K. Detecting non-Abelian statistics in the *v*=5/2 fractional quantum Hall state. *Phys. Rev. Lett.* **96**, 016803 (2006).
14. Clarke, D. J., Alicea, J. & Shtengel, K. Exotic non-Abelian anyons from conventional fractional quantum Hall states. *Nat. Commun.* **4**, 1348 (2013).
15. Lutchyn, R. M., Sau, J. D. & Das Sarma, S. Majorana fermions and a topological phase transition in semiconductor-superconductor heterostructures. *Phys. Rev. Lett.* **105**, 077001 (2010).
16. Willett, R. L., Nayak, C., Shtengel, K., Pfeiffer, L. N. & West, K. W. Magnetic-field-tuned Aharonov–Bohm oscillations and evidence for non-Abelian anyons at *v*=5/2. *Phys. Rev. Lett.* **111**, 186401 (2013).
17. Banerjee, M. et al. Observation of half-integer thermal Hall conductance. *Nature* **559**, 205–210 (2018).
18. Kasahara, Y. et al. Majorana quantization and half-integer thermal quantum Hall effect in a Kitaev spin liquid. *Nature* **559**, 227–231 (2018).
19. Dolev, M., Heiblum, M., Umansky, V., Stern, A. & Mahalu, D. Observation of a quarter of an electron charge at the *v* = 5/2 quantum Hall state. *Nature* **452**, 829–834 (2008).
20. Bartolomei, H. et al. Fractional statistics in anyon collisions. *Science* **368**, 173–177 (2020).
21. Dutta, B. et al. Distinguishing between non-Abelian topological orders in a quantum Hall system. *Science* **375**, 193–197 (2022).
22. Arute, F. et al. Quantum supremacy using a programmable superconducting processor. *Nature* **574**, 505–510 (2019).
23. Wu, Y. et al. Strong quantum computational advantage using a superconducting quantum processor. *Phys. Rev. Lett.* **127**, 180501 (2021).
24. Krinner, S. et al. Realizing repeated quantum error correction in a distance-three surface code. *Nature* **605**, 669–674 (2022).
25. Kim, Y. et al. Evidence for the utility of quantum computing before fault tolerance. *Nature* **618**, 500–505 (2023).
26. Ebadi, S. et al. Quantum phases of matter on a 256-atom programmable quantum simulator. *Nature* **595**, 227–232 (2021).
27. Zhong, H.-S. et al. Quantum computational advantage using photons. *Science* **370**, 1460–1463 (2020).
28. Madsen, L. S. et al. Quantum computational advantage with a programmable photonic processor. *Nature* **606**, 75–81 (2022).
29. Egan, L. et al. Fault-tolerant control of an error-corrected qubit. *Nature* **598**, 281–286 (2021).
30. Moses, S. A. et al. A race-track trapped-ion quantum processor. *Phys. Rev. X* **13**, 041052 (2023).
31. Dumitrescu, P. T. et al. Dynamical topological phase realized in a trapped-ion quantum simulator. *Nature* **607**, 463–467 (2022).
32. Zhang, X. et al. Digital quantum simulation of Floquet symmetry-protected topological phases. *Nature* **607**, 468–473 (2022).
33. Satzinger, K. et al. Realizing topologically ordered states on a quantum processor. *Science* **374**, 1237–1241 (2021).
34. Semeghini, G. et al. Probing topological spin liquids on a programmable quantum simulator. *Science* **374**, 1242–1247 (2021).
35. Andersen, T. I. et al. Non-Abelian braiding of graph vertices in a superconducting processor. *Nature* **618**, 264–269 (2023).
36. Xu, S. et al. Digital simulation of projective non-Abelian anyons with 68 superconducting qubits. *Chinese Phys. Lett.* **40**, 060301 (2023).
37. Iqbal, M. et al. Creation of non-Abelian topological order and anyons on a trapped-ion processor. *Nature* **626**, 505–511 (2024).
38. Hormozi, L., Zikos, G., Bonesteel, N. E. & Simon, S. H. Topological quantum compiling. *Phys. Rev. B* **75**, 165310 (2007).
39. Etingof, P., Rowell, E. & Witherspoon, S. Braid group representations from twisted quantum doubles of finite groups. *Pac. J. Math.* **234**, 33–41 (2008).

40. Lin, C.-H., Levin, M. & Burnell, F. J. Generalized string-net models: a thorough exposition. *Phys. Rev. B* **103**, 195155 (2021).

41. Freedman, M. H., Larsen, M. & Wang, Z. A modular functor which is universal for quantum computation. *Comm. Math. Phys.* **227**, 605–622 (2002).

42. Hu, Y., Geer, N. & Wu, Y.-S. Full dyon excitation spectrum in extended Levin-Wen models. *Phys. Rev. B* **97**, 195154 (2018).

43. Nemkov, N. A., Kiktenko, E. O., Luchnikov, I. A. & Fedorov, A. K. Efficient variational synthesis of quantum circuits with coherent multi-start optimization. *Quantum* **7**, 993 (2023).

44. Liu, Y.-J., Shtengel, K., Smith, A. & Pollmann, F. Methods for simulating string-net states and anyons on a digital quantum computer. *PRX Quantum* **3**, 040315 (2022).

45. Kitaev, A. & Preskill, J. Topological entanglement entropy. *Phys. Rev. Lett.* **96**, 110404 (2006).

46. Levin, M. & Wen, X.-G. Detecting topological order in a ground state wave function. *Phys. Rev. Lett.* **96**, 110405 (2006).

47. Flammia, S. T., Hamma, A., Hughes, T. L. & Wen, X.-G. Topological entanglement Rényi entropy and reduced density matrix structure. *Phys. Rev. Lett.* **103**, 261601 (2009).

48. Elben, A., Vermersch, B., Dalmonte, M., Cirac, J. I. & Zoller, P. Rényi entropies from random quenches in atomic Hubbard and spin models. *Phys. Rev. Lett.* **120**, 050406 (2018).

49. Brydges, T. et al. Probing Rényi entanglement entropy via randomized measurements. *Science* **364**, 260–263 (2019).

50. Eisert, J., Cramer, M. & Plenio, M. B. Colloquium: area laws for the entanglement entropy. *Rev. Mod. Phys.* **82**, 277 (2010).

51. Yang, C. N. & Ge, M. L. *Braid Group, Knot Theory and Statistical Mechanics* (World Scientific, 1991).

52. Kitaev, A. Anyons in an exactly solved model and beyond. *Ann. Phys.* **321**, 2–111 (2006).

53. Fan, Y.-A. et al. Experimental quantum simulation of a topologically protected Hadamard gate via braiding Fibonacci anyons. *Innovation* **4**, 100480 (2023).

54. Schotte, A., Zhu, G., Burgelman, L. & Verstraete, F. Quantum error correction thresholds for the universal Fibonacci Turaev-Viro code. *Phys. Rev. X* **12**, 021012 (2022).

55. Hahn, A. & Wolf, R. Generalized string-net model for unitary fusion categories without tetrahedral symmetry. *Phys. Rev. B* **102**, 115154 (2020).

56. Heinrich, C., Burnell, F., Fidkowski, L. & Levin, M. Symmetry-enriched string nets: exactly solvable models for set phases. *Phys. Rev. B* **94**, 235136 (2016).

57. Barter, D., Bridgeman, J. C. & Wolf, R. Computing associators of endomorphism fusion categories. *SciPost Phys.* **13**, 029 (2022).

58. D'Agostini, G. A multidimensional unfolding method based on Bayes' theorem. *Nucl. Instrum. Methods Phys. Res., Sect. A* **362**, 487–498 (1995).

59. Nachman, B., Urbanek, M., A. de Jong, W. & W. Bauer, C. Unfolding quantum computer readout noise. *npj Quantum Inf.* **6**, 84 (2020).

Methods

Fixed-point wavefunction

The Hamiltonian in equation (1) of the string-net model is designed to capture the most essential fixed-point wavefunctions, which are superpositions of various string-net configurations. These configurations are characterized by the geometry and the types of an ensemble of strings. The fixed-point wavefunction captures the universal properties of the string-net condensed phases in (2+1) dimensions, which can describe all the so-called 'doubled' topological phases. Here we present the exact ground-state wavefunction in the string-net picture and the corresponding quantum state simulated on physical qubits. Denoting the wavefunction as Φ, it is uniquely specified by the following four local constraints[6]:

$$\Phi\left(\begin{array}{c} a \end{array} \right) = \Phi\left(\begin{array}{c} a \end{array} \right), \qquad (5a)$$

$$\Phi\left(\begin{array}{c} a \end{array} \right) = d_a \Phi\left(\begin{array}{c} \ \end{array} \right), \qquad (5b)$$

$$\Phi\left(\begin{array}{c} a\ \overset{d}{}\ c \\ b \end{array} \right) = \delta_{ac}\Phi\left(\begin{array}{c} a\ \overset{d}{}\ a \\ b \end{array} \right), \qquad (5c)$$

$$\Phi\left(\begin{array}{c} a\ \overset{e}{\times}\ d \\ b\quad c \end{array} \right) = \sum_f F^{abe}_{cdf}\Phi\left(\begin{array}{c} a\qquad d \\ b\ f\ \ c \end{array} \right), \qquad (5d)$$

where the shaded regions represent arbitrary string-net configurations. d_a is the quantum dimension of string type a and the six-index tensor F has a one-to-one correspondence to the doubled topological phases. Since we only consider the self-dual model in this work, all the string configurations discussed here are unoriented. The wavefunction Φ is precisely the ground state of the Hamiltonian in equation (1).

According to these local constraints, the general value of Φ can be exactly calculated for any string-net configurations. For a given geometry g, the wavefunction Φ becomes a function of string types $\{s\}$. For example,

$$\Phi\left(g = \square, s_1 = a \right) = \Phi\left(\begin{array}{c} a \end{array} \right) = d_a \Phi\,(\text{vacuum}) = d_a. \qquad (6)$$

where $\Phi(\text{vacuum}) = 1$ following the notation from another work[40]. One can also calculate the amplitudes of different string types on two independent loops:

$$\Phi\left(g = \square\square, s_1 = a, s_2 = b \right) = \Phi\left(\begin{array}{cc} a & b \end{array} \right)$$
$$= d_a d_b \Phi\,(\text{vacuum}) = d_a d_b. \qquad (7)$$

From these two examples, we see that the wavefunction Φ can be recognized as a function to represent the linear relations between different string-net configurations. Once the geometry of the configuration is determined, it becomes a function of string types.

In the quantum circuit scheme, we simulate the linear relations described by symbol F, which corresponds to multi-controlled unitary gates (Fig. 2b). From equation (5d), the F move changes the type of one string according to its four connected strings, which is a five-qubit gate. We can use a simplified quantum circuit to realize the F move when there is some prior information on the string-net configuration (Fig. 2). Here we denote the quantum circuit corresponding to the complete and simplified F move as C_F for brevity, whereas a detailed description can

be found in Supplementary Section II.B. Now we give the quantum state that simulates the state Φ with the geometry $g = 1$ loop. For the Fibonacci string-net model, $\Phi_1(s_1 = 0) = d_0 = 1$ and $\Phi_1(s_1 = 0) = d_1 = \phi$ according to equation (6). The corresponding normalized quantum state reads[60,61]

$$|G_1\rangle = \frac{1}{\sqrt{1+\phi^2}}\left(|0\rangle + \phi\,|1\rangle \right) = U_S\,|0\rangle, \qquad (8)$$

where $U_S = \frac{1}{\sqrt{1+\phi^2}}\begin{pmatrix} 1 & \phi \\ \phi & -1 \end{pmatrix}$. More precisely, the state Φ under the geometry of one isolated loop is

$$\Phi\left(g = \square \right) = \Phi_1\,(s_1) = \frac{\langle s_1\,|G_1\rangle}{\langle 0\,|G_1\rangle}, \qquad (9)$$

where $\langle 0|G_1\rangle$ on the denominator is for the consistency with $\Phi(\text{vacuum}) = 1$ (ref. 40).

Similarly, we can simulate the wavefunction Φ of two independent loops with $|G_2\rangle = U_S|0\rangle \otimes U_S|0\rangle$. Now, we consider a more complex geometry of the two connected loops:

$$\Phi\left(a\square c\square b \right) = \sum_j F^{bac}_{abj}\Phi\left(a\square\overset{j}{\text{—}}\square b \right)$$
$$= \sum_j F^{bac}_{abj}\delta_{j0}\Phi\left(\begin{array}{cc} a & b \end{array} \right)$$
$$= F^{bac}_{ab0}d_a d_b. \qquad (10)$$

The corresponding quantum state in the quantum circuit scheme is

$$|G_{abc}\rangle = C_F\,|G_3\rangle = C_F\,(|G_2\rangle \otimes |0\rangle)$$
$$= C_F\,(U_S\,|0\rangle \otimes U_S\,|0\rangle \otimes |0\rangle), \qquad (11)$$

where $|G_2\rangle$ corresponds to the configuration of two isolated string loops a and b, $|G_3\rangle$ corresponds to the configuration of two string loops a and b connected by string j and C_F is the quantum circuit corresponds to F^{bac}_{ab0} in equation (10).

A simplified string-net wavefunction representation under the geometry shown in Fig. 2 can be expressed as

$$\Phi\left(\begin{array}{c} \text{(hexagonal configuration)} \end{array} \right)$$
$$= F^{cai_3}_{i_1 i_2 b}\Phi\left(\begin{array}{c} \text{(configuration)} \end{array} \right)$$
$$= F^{cai_3}_{i_1 i_2 b}F^{cbi_2}_{bc0}\Phi\left(\begin{array}{c} \text{(configuration)} \end{array} \right)$$
$$= F^{cai_3}_{i_1 i_2 b}F^{cbi_2}_{bc0}F^{bai_1}_{ab0}\Phi\left(\begin{array}{c} \text{(configuration)} \end{array} \right)$$
$$= F^{cai_3}_{i_1 i_2 b}F^{cbi_2}_{bc0}F^{bai_1}_{ab0}d_a d_b d_c. \qquad (12)$$

In the quantum circuit scheme, the initialization of an independent polygon can be realized by implementing U_S first, and then entangling the remaining strings of this polygon by CNOT gates controlled by the qubits to which U_S applies. We call this operation as a 'copy' since this operation prepares multiple qubits to the same quantum state corresponding to the same string type. To merge the separated hexagons, we use the type-0 strings to connect them and use F moves to obtain the desired geometry, similar to the process shown in equation (10). As shown in Fig. 2, the first F move $F^{bai_1}_{ab0}$ and the second F move $F^{cbi_2}_{bc0}$ are realized by a three-qubit gate since there are two repetitive indexes for each of them. The last F move $F^{cai_3}_{i_1i_2b}$ is realized by a five-qubit gate as the general case. The number of edges changes in equation (12), where we add/remove auxiliary qubits to/from the corresponding quantum circuit accordingly. The decomposed circuits of the other multi-qubit gates corresponding to the F move and the methods to remove qubits are described in Supplementary Section II.B.

Fixed-point Hamiltonian

An exactly solvable lattice spin Hamiltonian has been introduced[6] in the form of equation (1) with the fixed-point wavefunction Φ as the ground state. In this Hamiltonian, the Q_v operator is defined as

$$Q_v|ijk\rangle_v = \delta_{ijk}|ijk\rangle_v, \tag{13}$$

where the wavefunction $|ijk\rangle_v$ represents the types of three strings meeting at vertex v, and the tensor δ_{ijk} corresponds to the fusion rules for specific anyons. For the Fibonacci anyon, valid fusion rules are

$$\mathbf{1} \times \mathbf{1} = \mathbf{1}, \mathbf{1} \times \tau = \tau \times \mathbf{1} = \tau, \tau \times \tau = \mathbf{1} + \tau, \tag{14}$$

which gives $\delta_{ijk} = 1$ if $ijk \in \{000, 011, 101, 110, 111\}$ and $\delta_{ijk} = 0$ otherwise[54].

Meanwhile, B_p corresponds to the local constraints in equations (5a)–(5d) that uniquely specify the wavefunction capturing the properties of topologically ordered states. It is a sum of closed string operators describing particle and antiparticle pairs created from vacuum, moved along the edges of a plaquette (Fig. 1b), and annihilated back to vacuum. In the Fibonacci string-net model, B_p is defined as

$$B_p = \frac{1}{1+\phi^2}\left(B^0_p + \phi B^1_p\right), \tag{15}$$

where $s \in \{0, 1\}$ represents the string types. B^s_p changes the state on the six edges of the plaquette p controlled by the state on the six outer links of p. The explicit algebraic form of B^s_p is presented in the 'String operators' section as the smallest closed string operator along the edge of one plaquette, which describes the process of creating a pair of type-s anyons, moving around this plaquette and fusing to vacuum.

String operators

The quasiparticle excitations live at the endpoints of the string operators. In Fig. 1c, we illustrate how the F and R moves extend the string operator and turn its direction. Here we give the explicit algebraic form to create, move and fuse these quasiparticle excitations in the string-net picture. In the main text, we have mentioned that we use the tailed string-net picture[42] where the tails represent the quasiparticle excitations located at the endpoints of the string operator. We also use this picture to conveniently describe the creation and fusion of these excitations.

As shown in Extended Data Fig. 3a, the creation of a pair of type-s excitations from vacuum can be described as adding a short type-s open string. Since one can erase or add the null (vacuum) strings at will[40,52], the type-s open string is connected to the string net by the null string. Then, we use one F move to turn this configuration into a tailed string net where the endpoints of the string operator are well defined. The fusion of these excitations can be implemented by connecting the tails with F move (Extended Data Fig. 3b). Under this framework, the

algebraic form of the string operator is the same as that in ref. 6 for moving quasiparticles. The creation and fusion are defined near the endpoints of the string operator and exhibit some ambiguity, which is not important for our purposes since it does not affect the braiding statistics of the excitations[40]. For the closed string operators, the creation and fusion operation will introduce a constant factor related to the quantum dimension of type-s string, as discussed in more detail subsequently.

We consider the closed string operator B^s_p, which can be regarded as creating a pair of type-s excitations from vacuum, winding them around in this plaquette, and then annihilating them to the vacuum. As shown in Extended Data Fig. 4, we create a pair of type-s excitations at string a with $F^{ss0}_{aaa'}$. Then, we move the tail on the left around this plaquette with $F^{gba}_{sa'b'}\cdots F^{laf}_{sf'a'}$. Finally, we annihilate these two excitations to vacuum with $F^{sa'a}_{a's0}$. According to the normalization convention[6], $F^{ss0}_{aaa'} = \frac{v_{a'}}{v_sv_a}\delta_{saa'}$ and $F^{sa'a}_{a's0} = \frac{v_a}{v_sv_{a'}}\delta_{saa'}$, where v represents the square root of the quantum dimension d. The product of these two terms is a constant factor $1/d_s$, which is eliminated by equation (5b) considering the fact that B^s_p create a type-s closed loop. The type-s string operator on this plaquette can be expressed as

$$\left\langle \begin{matrix} i & & d' & j \\ h & c' & & e' & k \\ & b' & & f' & \\ g & & a' & l \end{matrix} \middle| B^s_p \middle| \begin{matrix} i & & d & j \\ h & c & & e & k \\ & b & & f & \\ g & & a & l \end{matrix} \right\rangle =$$

$$F^{gba}_{sa'b'} F^{hcb}_{sb'c'} F^{idc}_{sc'd'} F^{jed}_{sd'e'} F^{kfe}_{se'f'} F^{laf}_{sf'a'}, \tag{16}$$

where B^s_p does not change the types of the six outgoing strings connected to the hexagon.

As the endpoints of the string operator, the tails always have a definite string type that matches the type of the corresponding string operator. Consequently, we do not attach physical qubits to the tails since there is no degree of freedom for their types. However, the tails representing the fusion results have multiple values for non-Abelian anyons and require to be captured by physical qubits (Fig. 4 and Extended Data Fig. 3). For example, in the implementation of (closed) string operator B^s_p, the first movement of excitation is implemented by $F^{gba}_{sa'b'}$. Although it has six indexes, the value of s is predetermined as the type of the simple string operator and does not occur in the quantum circuit scheme. The most complicated part in the circuit implementation of simple string operators is to apply four-qubit gates, different from the cases of preparing the ground state and the projective measurement of the plaquette operator B_p where five-qubit gates are involved[44,62]. A more detailed description to implement these multi-qubit gates is given in Supplementary Section II.

Fusion space

Non-Abelian anyons have multiple fusion outputs and can be used for constructing the topologically protected logical qubits. In this work, we use four Fibonacci anyons with the vacuum total charge to encode one logical qubit. The measurement results of the logical qubit can be obtained by measuring the fusion outcomes of the first or last two anyons. The fusion results of the first and last two anyons should be the same according to charge conservation[36]. The quantum gates implemented on logical qubits are realized by the braiding operators, whose matrix representations are associated with the encoding scheme. A common calculation method is through the fusion tree notation[63].

The braiding operator σ_1 in our encoding scheme of $|\bar{0}\rangle = |(\tau \times \tau)_\mathbf{1}, (\tau \times \tau)_\mathbf{1}\rangle$ and $|\bar{1}\rangle = |(\tau \times \tau)_\tau, (\tau \times \tau)_\tau\rangle$ can be calculated by the R matrix of Fibonacci theory as

$$\sigma_1 |x\rangle = \left| \begin{matrix} \tau & \tau & \tau \\ & & \\ x & & \tau \end{matrix} \right\rangle = R^x_{\tau\tau} \left| \begin{matrix} \tau & \tau & \tau \\ & & \\ x & & \tau \end{matrix} \right\rangle = R^x_{\tau\tau} |x\rangle. \tag{17}$$

Furthermore, the braiding operator σ_2 is calculated by the F and R matrices of Fibonacci theory as

$$
\begin{aligned}
\sigma_2 \left| x \right\rangle &= \left| \begin{array}{c} \tau \ \tau \ \tau \\ x \ \tau \end{array} \right\rangle = \sum_y F^{\tau\tau x}_{\tau\tau y} \left| \begin{array}{c} \tau \ \tau \ \tau \\ y \ \tau \end{array} \right\rangle \\
&= \sum_y R^y_{\tau\tau} F^{\tau\tau x}_{\tau\tau y} \left| \begin{array}{c} \tau \ \tau \ \tau \\ y \ \tau \end{array} \right\rangle \\
&= \sum_y F^{\tau\tau y}_{\tau\tau z} R^y_{\tau\tau} F^{\tau\tau x}_{\tau\tau y} \left| \begin{array}{c} \tau \ \tau \ \tau \\ z \ \tau \end{array} \right\rangle \\
&= \sum_y F^{\tau\tau y}_{\tau\tau z} R^y_{\tau\tau} F^{\tau\tau x}_{\tau\tau y} \left| z \right\rangle .
\end{aligned}
\tag{18}
$$

According to the matrix representations of the F and R move, $\sigma_1 = \begin{pmatrix} e^{-4\pi i/5} & 0 \\ 0 & e^{3\pi i/5} \end{pmatrix}$ and $\sigma_2 = \begin{pmatrix} \phi^{-1} e^{4\pi i/5} & \phi^{-1/2} e^{-3\pi i/5} \\ \phi^{-1/2} e^{-3\pi i/5} & -\phi^{-1} \end{pmatrix}$. In the logical space, processes (2)–(5) (Fig. 4c(ii)–(v), respectively) are expressed as

$$
\sigma_2 \left| \bar{0} \right\rangle = \phi^{-1} e^{4\pi i/5} \left| \bar{0} \right\rangle + \phi^{-1/2} e^{-3\pi i/5} \left| \bar{1} \right\rangle ,
\tag{19a}
$$

$$
\sigma_1 \sigma_2 \left| \bar{0} \right\rangle = \phi^{-1} \left| \bar{0} \right\rangle + \phi^{-1/2} \left| \bar{1} \right\rangle ,
\tag{19b}
$$

$$
\sigma_2 \sigma_1 \sigma_2 \left| \bar{0} \right\rangle = \phi^{-1} e^{-4\pi i/5} \left| \bar{0} \right\rangle + \phi^{-1/2} e^{-4\pi i/5} \left| \bar{1} \right\rangle ,
\tag{19c}
$$

$$
\sigma_2^2 \left| \bar{0} \right\rangle = -\phi^{-2} \left| \bar{0} \right\rangle + \sqrt{3\phi - 4}\, e^{3\pi i/10} \left| \bar{1} \right\rangle ,
\tag{19d}
$$

respectively.

We notice that equation (19d) describes a three-step process defining the elements M_{ab} of the monodromy matrix[40]: (1) create two particle–antiparticle pairs $(a, \bar{a}, b, \bar{b})$ from vacuum; (2) braid particle a around particle b; and (3) annihilate both pairs to the vacuum, which is exactly the process shown in Fig. 4c(v). In the Fibonacci string-net model, the amplitude of the logical $\left| \bar{0} \right\rangle$ measured in process (5) gives the value of $M_{\tau\tau}$, denoted as $M_{\tau\tau} = \langle \bar{0} | \sigma_2 \sigma_2 | \bar{0} \rangle$. By the theory of modular tensor category[64], the element $M_{\tau\tau}$ is a real negative value taking the form of $-1/d^2$, where d is the quantum dimension of the quasiparticle excitation. In our experiment, we obtain $M_{\tau\tau} \approx -0.39$, which is the negative square root of the experimentally measured probability for the state $\left| 00 \right\rangle$ in Fig. 4d(v). Consequently, an experimental estimation for the quantum dimension of the Fibonacci anyon is $d_\tau = \sqrt{-1/M_{\tau\tau}} \approx 1.60$.

Circuit implementation

The original circuits for preparing the ground state and realizing different types of F move are compiled to fit the native gate set (that is, arbitrary single-qubit gates and two-qubit CZ gates) and the layout geometry of the processor. We tackle this problem by exploiting the variational unitary synthesis technique, which can be divided into a discrete optimization part searching for the best circuit architecture and a continuous optimization part finding the best set of single-qubit rotation angles. In practice, we adopt the recently introduced CPFlow package[43] to design the desired circuits.

The circuits for ground-state preparation and anyon braiding in this work are composed of scalable modules and can be optimized by blocks. In addition, for the ground-state preparation, we can further set the state vector of the ground state as the target and optimize the circuit as a whole, which further reduces the circuit depth. Before running the circuit, further alignments are executed to reduce the impact of decoherence errors, and Carr–Purcell–Meiboom–Gill gates are inserted to echo low-frequency noises. The experimental circuits for preparing the ground state are explicitly displayed in Supplementary Section III.B.

Randomized measurement

In our experiment, we adopt the randomized measurement method to obtain the second-order Rényi entropies and calculate the topological entanglement entropy[33,48,49]. This method is achieved by applying random unitaries, which are products of single-qubit unitaries sampled from the circular unitary ensemble, to the system and measuring the final states on the computational basis. For each instance of random unitaries, we repeat the measurement many times to sample the probabilities of the bit strings. The second-order Rényi entropy can be computed as

$$
\begin{aligned}
S_2(\rho_A) &= -\ln(\mathrm{Tr}(\rho_A^2)) \\
&= -\ln(2^{N_A} \sum_{w,w'} (-2)^{-H(w,w')} \overline{P(w)P(w')}),
\end{aligned}
\tag{20}
$$

where N_A and ρ_A are the qubit number and density matrix of system A, respectively. Here w and w' are the binary strings and $H(w, w')$ is the Hamming distance between them. $P(w)$ denotes the probability of observing w. The average is over different instances of random unitaries in randomized measurement. During the calculation, we also use the iterative Bayesian unfolding scheme to mitigate measurement errors and alleviate undersampling bias (Supplementary Section III.D).

After preparing the ground state, we apply random unitaries to an 18-qubit system and measure its final state, from which we can obtain the second-order Rényi entropies of all the subsystems described in the main text. In practice, we find that an instance number of 1,500 and a sampling number of 300,000 for each instance are required to provide a reliable estimate of the second-order Rényi entropy of an 11-qubit subsystem. Supplementary Section III.C provides more details on the choices of the number of instances as well as the tomography verification of the randomized measurement method with small systems.

Data availability

The data presented in the figures and that support the other findings of this study are publicly available via Figshare at https://doi.org/10.6084/m9.figshare.24947646 (ref. 65).

Code availability

The data analysis and numerical simulation codes for this study are publicly available via Figshare at https://doi.org/10.6084/m9.figshare.24947646 (ref. 65).

References

60. Buerschaper, O., Aguado, M. & Vidal, G. Explicit tensor network representation for the ground states of string-net models. *Phys. Rev. B* **79**, 085119 (2009).
61. Gu, Z.-C., Levin, M., Swingle, B. & Wen, X.-G. Tensor-product representations for string-net condensed states. *Phys. Rev. B* **79**, 085118 (2009).
62. Bonesteel, N. E. & DiVincenzo, D. P. Quantum circuits for measuring Levin-Wen operators. *Phys. Rev. B* **86**, 165113 (2012).
63. Field, B. & Simula, T. Introduction to topological quantum computation with non-Abelian anyons. *Quantum Sci. Technol.* **3**, 045004 (2018).
64. Rowell, E., Stong, R. & Wang, Z. On classification of modular tensor categories. *Commun. Math. Phys.* **292**, 343–389 (2009).
65. Xu, S. et al. Non-Abelian braiding of Fibonacci anyons with a superconducting processor. *Figshare* https://doi.org/10.6084/m9.figshare.24947646 (2024).

Acknowledgements

Author contributions

S.X. and K.W. carried out the experiments under the supervision of C.S. and H.W. J.C. and X. Zhu. designed the device and H.L. fabricated the device, supervised by H.W. Z.-Z.S. designed the quantum circuits under the supervision of D.-L.D. W.L., W.J., L.-W.Y., Z.-Z.S. and D.-L.D. conducted the theoretical analysis. All authors contributed to the experimental setup, analysis of data, discussions of the results and writing of the manuscript.

Competing interests

The authors declare no competing interests.

Additional information

Extended data is available for this paper at https://doi.org/10.1038/s41567-024-02529-6.

Supplementary information The online version contains supplementary material available at https://doi.org/10.1038/s41567-024-02529-6.

Correspondence and requests for materials should be addressed to Chao Song, H. Wang or Dong-Ling Deng.

Peer review information *Nature Physics* thanks Arpit Dua, Carolin Wille and the other, anonymous, reviewer(s) for their contribution to the peer review of this work.

Reprints and permissions information is available at www.nature.com/reprints.
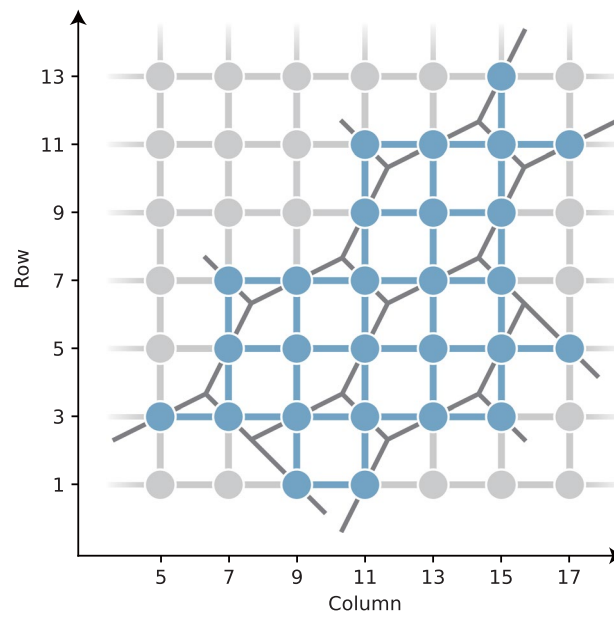
Extended Data Fig. 1 | The layout of the 27 qubits (blue circles) used in our experiments, based on which we construct the desired honeycomb lattice. The neighboring qubits are connected with tunable couplers denoted as bars. Each physical qubit is labeled by $Q_{(i,j)}$ with $i(j)$ being the row (column) index.
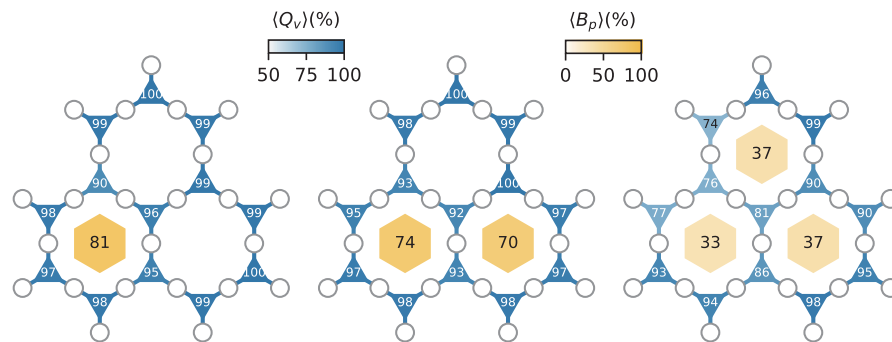
Extended Data Fig. 2 | The measured expectation values of the vertex (Q_v) and plaquette (B_p) operators after step 1 (left), 2 (middle) and 3 (right). A repetition number of 3000 (300,000) is used to obtain the probability distributions in the computational basis, which are corrected with iterative Bayesian unfolding methods[58,59] to mitigate readout error for calculating $\langle Q_v \rangle$ ($\langle B_p \rangle$) (Fig. 2a).
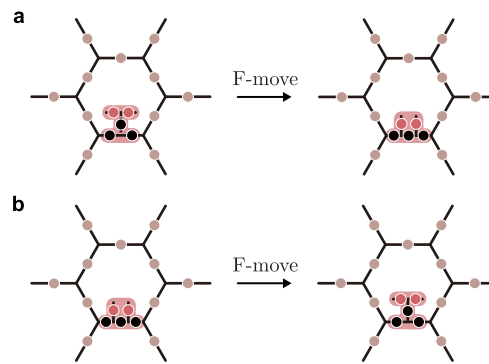
Extended Data Fig. 3 | Creation and fusion of the quasiparticle excitations. **a**, To create a pair of quasiparticles, we add a short string on the string-net configuration. It can be regarded as connected to the honeycomb lattice with the vacuum string, which can be arbitrarily added and removed. One F-move acting on the type-s string, the type-0 connecting string, and the nearby edge can change the fattened lattice picture[6] to the tailed string-net picture. **b**, To annihilate (fuse) two quasiparticles, we detach the two tails with one F-move to directly connect them. The string connecting these two detached tails indicates the fusion result of these two quasiparticles.
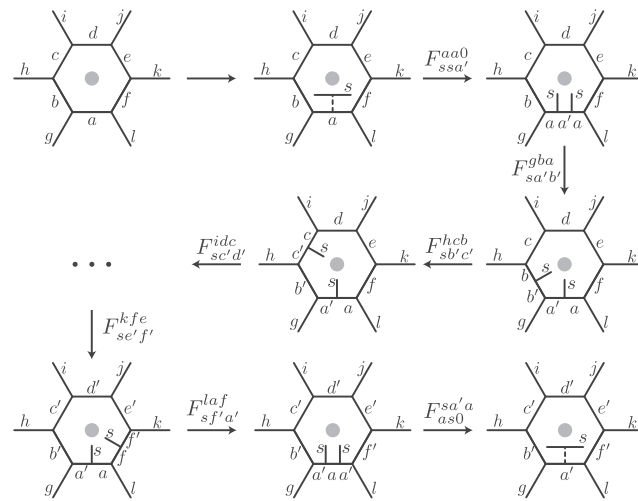
Extended Data Fig. 4 | The process described by B_p^s as a closed string operator. The effect of B_p^s can be understood as creating a pair of type-s excitations from vacuum, moving the excitations around this plaquette, and annihilating them to vacuum. Under the tailed string-net picture, the positions of the tails clearly reveal this process. In this figure, we only move the tail initialized on the left. However, different schemes of moving these tails along this path do not change the algebraic representation of the closed string operator B_p^s according to Mac Lane's coherence theorem[52].